Vertical velocity of acoustic wave determined from altitudes of TEC disturbances after a foreshock of the 2011 Tohoku Earthquake

Yoshihiro Kakinami[1, 2], Hiroaki Saito[3, 4], Tetsuo Yamamoto[4], Chia-Hung Chen[5], Masa-yuki Yamamoto[3], Kensuke Nakajima[6], Jann-Yenq Liu[7] and Shigeto Watanabe[1]

[1]Hokkaido Information University, Ebetsu, Hokkaido 069-8585, Japan

[2]National Institute of Technology, Tomakomai College, Tomakomai, Hokkaido 059-1275, Japan

[3]Kochi University of Technology, Kami, Kochi 782-8502, Japan

[4]Hokkaido University, Sapporo, Hokkaido 060-0808, Japan

[5]National Cheng Kung University, Tainan 701, Taiwan

[6]Kyushu University, Fukuoka 819-0395, Japan

[7]National Central University, Taoyuan 32001, Taiwan

Corresponding author: Yoshihiro Kakinami (kakinami@do-johodai.ac.jp)

Key Points:

- A method of determining geographic coordinates and altitudes of ionospheric disturbance detected in TEC is proposed.
- The ionospheric disturbances in TEC were found to be below the F2-peak at the foreshock of the 2011 Tohoku Earthquake on 9 March 2011.
- A fast acoustic wave was detected form the TEC analysis after the foreshock of the 2011 Tohoku Earthquake

Abstract

We investigate ionospheric disturbances using the total electron content (TEC) data retrieved by the three satellites after the foreshock of the 2011 Tohoku Earthquake on 9 March 2011. Co-seismic ionospheric disturbances (CIDs) appeared to extend from an onset point concentrically in all of the satellite data. We have found, however, that the geographic coordinates of the onset points did not coincide if the observed CIDs were assumed to occur at one altitude. Admitting that the altitudes of the onset points are different, we searched for coinciding geographic coordinates of the onset points using the two data sets by changing the altitudes and identified the altitude of the two onset points at 155.4 and 234.9 km, and the onset time at these altitudes. As a result, the vertical velocity of acoustic wave is estimated to be 1.04 km/s from the travel time between the altitudes of 155.4 and 234.9 km. This is 1.4 times higher than the sound velocity calculated using the empirical model NRLMSISE-00. The present study provides a method of determining the source location of the acoustic wave from the ionospheric TEC analysis without using the seismic data.

1 Introduction

An altitude of the observation of total electron content (TEC) obtained by the global navigation satellite system (GNSS) is inherently uncertain because TEC is the plasma density integrated along the ray path between a satellite and a ground-based receiver. In many reports on the TEC analyses, the altitude of TEC disturbance is assumed to be the F2-peak altitude around 300 km, where the plasma density is the highest there. However, TEC disturbances do not always represent the plasma disturbance at the F2-peak. For example, *Maeda and Heki* [2014] found that the TEC disturbances caused by a sporadic E layer were at 106 km altitude. They determined the observed altitude with the use of triangulation on the basis of the fact that the disturbances found in the different satellite data must coincide. Furthermore, a missile/rocket induces TEC disturbances above or below the F2-peak. *Ozeki and Heki* [2010] estimated the altitude of plasma depletion caused by the missile exhaust with triangulation of two data sets. *Kakinami et al*. [2013a] determined the altitude of disturbances induced by the missile assuming its trajectory. These results indicate that the assumption of the altitude at the F2-peak is not always valid.

Acoustic waves are often observed after earthquakes [e.g., *Bolt*, 1964; *Arai et al*., 2011] because motions of the ground and sea surface act as a huge loudspeaker. Acoustic waves reach the thermosphere and disturb ionospheric plasma through collisions and recombination. Co-seismic ionospheric disturbances (CIDs) are often observed in high-frequency (HF) Doppler measurements [e.g., *Leonard and Barns*, 1965; *Chum et al.*, 2012; *Liu et al*., 2016] and in TEC data obtained by the GNSS [e.g., *Ducic et al*., 2003]. For example, traveling CIDs and a large ionospheric hole occurred over the tsunami source area at 9 min after the 2011 Tohoku Earthquake on 11 March 2011 [*Kakinami et al*., 2012]. First, traveling CIDs associated with Rayleigh waves (~ 3 km/s) was observed. Subsequently, CIDs associated with acoustic waves with horizontal phase velocity of ~ 1 km/s emitted from the tsunami source area and gravity waves (~ 300 m/s) coupled with the tsunami were detected [e.g., *Liu et al*., 2011; *Kakinami et al*., 2013b; *Occhipinti et al*., 2013, *Astafyeva* 2019 and references therein]. Furthermore, even a ground motion with a small amplitude induced by the P-wave could lead to the emission of acoustic waves that disturb the ionosphere [*Nishitani et al*., 2011]. These results suggest that the

acoustic waves excited by earthquakes can be used to probe atmospheric properties and the underlying physics of the emission and propagation of acoustic waves in the atmosphere.

Various attempts have been made to estimate the vertical velocity of acoustic waves excited by earthquakes. *Liu et al*. [2016] attempted to determine it from a travel time between the ground to the altitude of CIDs with the use of the TEC data assuming the altitude of CIDs to be 350 km. *Astafyeva et al*. [2011] showed that disturbances propagated at supersonic speeds assuming the altitude of CIDs to be 250 km. However, the ambiguity in the altitude of the disturbances in the TEC data leads to uncertainty in the results of these studies. *Gracia et al*. [2005] have estimated the velocity of an acoustic wave excited by a Rayleigh wave by applying a tomographic method to the TEC data, but spatial and temporal resolutions of this method are limited. Ionosonde observations successfully probe the vertical profile of the disturbances induced by the acoustic wave [e.g., *Maruyama and Shinagawa*, 2014], but its poor time resolution limits the precision of the estimations of the vertical velocity of an acoustic wave.

In this paper, we propose a new method of determining the altitudes of the disturbance using the TEC data retrieved by the multiple satellites. Using the TEC data retrieved by PRN07, PRN08, and PRN10 at the foreshock of the 2011 Tohoku Earthquake occurred on 9 March 2011 (Mw 7.4, hereafter the Tohoku Foreshock), we shall show that the CIDs are not always observed at a fixed altitude and derive vertical velocity of the acoustic wave in the lower thermosphere.

2 Method of the data analysis and results

We analyzed the TEC data using a dual-frequency radio signal (1575.42 and 1222.60 MHz) from the GNSS after the Tohoku Foreshock. The 1-Hz GNSS data provided by the GNSS Earth Observation Network (GEONET) were smoothed to remove small noises in the raw data. Figure 1 shows an example of the TEC signals after performing the data smoothing. First, the raw data are smoothed using a 10-s running average. A 180-s running average is then applied to the 10-s running averaged data. Subtraction of the latter two data sets, which represent 10–180-s band-pass filtered data, are used in the analysis.

The exact geographic coordinates of the TEC disturbance cannot be determined unless the altitude of TEC disturbance is assumed. Figure 2 illustrates the geometry in determining the altitudes and locations of the ionospheric disturbances from the analysis of the TEC data. Assuming the altitude of the TEC disturbance observed by a satellite-receiver pair, we calculate a sub-ionospheric point (SIP) for the given pair, where SIP is a ground projection of the intersection of a line of sight and a horizontal plane of the assumed altitude. SIP would be close to the receiver if the altitude is assumed low, and vice versa.

Figure 3a–c shows snapshots of the CIDs observed by PRN07, PRN08, and PRN10 when each assumed altitude is set at 300 km. The elevation angles were approximately 30° for PRN07, 40° for PRN08, and 43° for PRN10. CIDs appeared to extend concentrically from a point in the three distributions. We call the center of the concentric pattern an onset point at the assumed altitude hereafter. The concentric patterns of CIDs are clearly seen in the data of PRN07 and PRN10, whereas they are less clear in PRN08.

Figure 3d–f displays typical time series of the band-pass-filtered TECs for PRN07, PRN08, and PRN10. In each of the panels, the TEC signals are displayed according to the ascending order of the distance between the onset point and SIP at the time of the mainshock.

We display here the data retrieved for 7 stations as representatives out of many stations shown in Figure 3a-c but the tendency is similar even if we include others as well. See movies in the supporting materials for the detailed time evolution of the CIDs. We assume the time of the first maximum in the filtered TEC (red dots in Figure 3d-f) to be the arrival time of the acoustic wave front in the south of the onset point. The earliest arrival time was 401 s after the main shock at 0179 station in PRN07, 490 s at 0916 station in PRN08, and 472 s at 0037 station in PRN10. For the CIDs in the north, on the other hand, the time of their enhancement was difficult to identify because of the lack of clear enhancement there due to the inclination of the geomagnetic field [c.f., *Astafyeva et al*., 2011; *Kakinami et al*., 2012, 2013b], so we assume the time of the maximum just before the rapid reduction to be the arrival time at the north of the onset point.

Figure 4 shows spatial distributions of the arrival time of the acoustic wave in the region near the epicenter for the assumed altitude of 300 km. The results for PRN07 and PRN10 show concentric patterns of the isochrones of the arrival time. However, it is evident that the onset points do not coincide. Furthermore, the isochrone has two local minima for PRN08 and the amplitude of the CIDs is smaller than those observed by PRN07 and PRN10. The data of PRN08 will note be used in the following analysis.

In the following, we shall show that we can find out coinciding geographical coordinates of the onset points obtained from PRN07 and PRN10 by relaxing the assumption of one fixed altitude of disturbance. Note that geographical coordinates of the onset points determined by different satellites should coincide. We use the data obtained at 130 GNSS stations for PRN07 and 138 GNSS stations for PRN10 for which the arrival times are determined clearly. We carried out the following procedure to identify the geographic coordinates of the coinciding onset points by varying the assumed altitudes.

(1) Assuming a tentative altitude of the TEC disturbance for each satellite, we calculate SIPs at the arrival time obtained from the various satellite-receiver pairs. Figure 4 shown in the previous section is an example of the results adopting a tentative altitude of 300 km.

(2) Form the SIPs tentatively obtained in the step (1) for each satellite, we determine a tentative onset point that gives the smallest root-mean-square error (RMSE) in the linear fitting for the relationship between the distances from the tentative onset point to the SIPs and the arrival times of the acoustic wave at the SIPs. We performed the grid search with the grid width of 1×10^{-3} degree in longitude and latitude. An example of the fitting result is shown in Figure 5 for the tentative altitude of 155 km for PRN07.

(3) We carry out steps (1) to (2) with varying the altitudes of the TEC disturbance for the two satellites, each in the ranges of 150-200 km for PRN07 and 200-240 km for PRN10, and search for the combination of the altitudes that gives the closest match of the geographic coordinates of the onset points determined by the two satellites.

Figure 6 shows the result of the search for the geographic coordinates of the onset points for the various tentative altitudes. The intersection of the red (PRN07) and blue (PRN10) lines is the point, where the two onset points determined by the PRN07 and PRN10 are projected onto the same location. Its geographic coordinates are given by 38.710°N and 143.457°E. The point is found to be located within 40 km from those of the maximum vertical displacement of the seafloor estimated from the seismic data [*Gusman et al*., 2013]. The observed altitudes of the CIDs are simultaneously determined to be 155.4 km for PRN07 and 234.9 km for PRN10. Figure 7 shows the spatial distributions of the arrival time of the acoustic wave at these altitudes. The

onset time for PRN07 and PRN10 are simultaneously found to be 399.9 s and 476.1 s by using the least-square fitting. Thus, the vertical velocity of acoustic wave averaged over the two altitudes is determined to be 1.04 km/s, which is faster by 40 % than that calculated with the use of NRLMSISE-00 [*Picone et al*., 2002], i.e. 0.73 km/s. This result indicates that the temperature was two times higher than that given by NRLMSISE-00 at the time of the earthquake. The results are summarized in Figure 8.

The horizontal neutral wind speed estimated from the horizontal wind model 1993 (HWM93) [*Hedin et al.,* 1996] is 6.72 m/s around the relevant altitude. If the effect of the wind on the acoustic wave is considered, the horizontal position of the onset point is shifted by 744 m, thus the horizontal neutral wind had little effect on the estimation of the vertical velocity of the acoustic wave. Figure 9 summarizes the results together with the configuration of the onset points of the CIDs, the satellites and the emission source of the acoustic wave.

The accuracy of the geographic coordinates of the onset point is the most critical factor for the altitude determination because it is directly linked to the accuracy of the obtained altitude. The distance between the location of the onset point and the nearest SIP is 22.2 km for PRN07 and 15.0 km for PRN10. If we take the nearest SIP for comparison, the altitude shifts by 14.3 km for PRN07 and 15.5 km for PRN10 compared with the one determined by the present method.

3 Summary and Discussion

We have analyzed the TEC data sets obtained by PRN07 and PRN10 GNSS satellites at the Tohoku Foreshock. The results exhibit a similar concentric pattern of the CIDs that appears to extend from the onset points in both data sets. We have demonstrated that, if we assume that the CIDs observed by PRN07 and PRN10 originated from one altitude, for example 300 km, the two onset points deviate largely with each other in the geographic coordinates (Figure 4). This implies that TEC disturbances should be located at various altitudes rather than a fixed altitude, suggesting that the altitude of the TEC disturbance must be carefully examined for each event. We have found that the coinciding geographic coordinates of the onset points in the data retrieved by PRN07 and PRN10 are possible (Figure 6). Its geographic coordinates are found to be close to the maximum vertical displacement of the seabed estimated from the seismic data analyses [*Gusman et al*., 2013], implying that the present method enables us to determine the source location of the acoustic wave independently from seismic data. The altitudes of the TEC disturbance are estimated to be 155.4 km for PRN07 and 234.9 km for PRN10, respectively. Our results indicate that the detectable onsets of the concentric pattern of the CIDs can occur below the F2-peak altitude, which has usually been assumed to be the observed altitude of CIDs. The vertical velocity of the acoustic wave is estimated to be 1.04 km/s around there from the differences of the altitudes and onset times deduced from the data retrieved from the two satellites. The velocity thus obtained is significantly faster than that of acoustic wave velocity calculated from the empirical model NRLMSISE-00.

One of the possible causes of the observed increase in the acoustic wave velocity is temperature elevation due to dissipation of the acoustic waves at those altitudes. Viscosity and thermal conduction result in energy dissipation of acoustic waves. Since the absorption coefficient α for a gas is inversely proportional to the gas density at low altitudes where the gas density is high [see e.g. *Landau and Lifshitz*, 1959], the amplitude of the acoustic wave increases

196 with increasing altitude at low altitudes. However, the amplitude decreases rapidly with
197 increasing altitudes above $\alpha\,\lambda \sim 1$ because of the dissipation, where λ is the wavelength of the
198 acoustic wave. Figure 10 shows $\alpha\,\lambda$ as a function of the altitude for the acoustic wave
199 frequencies where we used the expression of α given by *Landau and Lifshitz* [1959]. Figure 10
200 indicates that acoustic waves of frequency 0.1 Hz can reach up to ~200 km and dissipate rapidly
201 around this altitude. Note that the timescale of the fault motion of the earthquake was ~20 s
202 [United States Geological Survey,
203 https://earthquake.usgs.gov/earthquakes/eventpage/usp000hvhj/finite-fault], implying that the
204 dominant frequency of the acoustic waves emitted by this motion was ~0.1 Hz. Another
205 possibility is the limited degrees of freedom of motion of atmospheric molecules [*Pierce*, 2007
206 and references therein]. At low altitudes, where collision frequency of molecules is high, thermal
207 equilibrium is reached between the translational and the rotational energy distributions of N_2 and
208 O_2 molecules during the propagation of the acoustic wave. However, at high altitudes, where the
209 collision frequency is low, the thermal equilibrium breaks down for acoustic waves with high
210 frequencies because the relaxation time of the rotational energy distribution is longer than that of
211 the translational energy distribution. Consequently, the ratio of specific heat tends to increase
212 from 7/5 to 5/3 for a complete freeze of the rotational energy distribution. However, even if it
213 were possible, it would increase acoustic wave velocity by a factor of 1.1 at most compared with
214 the case of thermal equilibrium, and the velocity would still be less than that observed even in
215 this extreme case.

216 The CIDs after the Tohoku Foreshock have been reported by the previous studies.
217 *Thomas et al*. [2018] used the data of PRN07 and showed that the onset point for PRN07 was
218 located at the altitude of 130 km employing ray tracing calculations using the vertical profile of
219 neutral temperature given by NRLMSISE-00. They assumed that the source location of the
220 acoustic wave was at the geographic coordinates of the maximum vertical displacement of the
221 earthquake given by the seismic data. However, the altitude determined by the ray tracing has an
222 ambiguity originating from uncertainties in the vertical profile of neutral temperature and wind,
223 in particular, if one takes dissipation of the acoustic wave into account as discussed above.
224 *Astafyeva and Shults* [2019] also assumed that the location of the source of the acoustic wave at
225 the epicenter given by the seismic data. They ignored the difference of the altitudes of the onset
226 points for PRN07 and PRN10 without distinguishing the difference of the onset times and
227 obtained the onset altitude of 190 km just by comparing the locations of the onset points with the
228 epicenter. It should be pointed out that these two studies assumed the source location of the
229 acoustic wave by employing the seismic data. On the other hand, the present method uses only
230 ionospheric TEC data and is independent of the seismic data. Besides, the present method
231 provides a self-consistent way of determining both observed altitudes and source location of the
232 acoustic wave.

233 Measurements of acoustic wave velocity in the upper atmosphere were carried out with
234 the use of a rocket experiment using a grenade [e.g., *Stroud et al*., 1960]. Even in this type of
235 experiment, however, one can obtain only the acoustic wave velocity averaged over the altitudes
236 from the ground to the lower thermosphere. Recently, direct observation of an acoustic wave in
237 the upper atmosphere was made using a high-precision barometer onboard a sounding rocket
238 [*Kihara et al*., 2014], although this method has not yet been fully established. The present
239 method we hope provides a tool for determining the acoustic wave velocity in the thermosphere.
240 Furthermore, the method helps to link both seismological and acoustic wave observations, which

241 we hope will lead to a deeper understanding of the emission and propagation mechanisms of
242 acoustic waves triggered by an earthquake.

243

244 **Acknowledgments**

245 We thank that the Geospatial Information Authority of Japan for the GEONET RINEX data
246 (ftp://terras.gsi.go.jp/), HWM93 (https://ccmc.gsfc.nasa.gov/modelweb/atmos/hwm.html), and
247 for NRLMSISE-00 (https://ccmc.gsfc.nasa.gov/pub/modelweb/atmospheric/msis/) and United
248 States Geological Survey (https://earthquake.usgs.gov/earthquakes/eventpage/usp000hvhj/finite-
249 fault) for the information of the foreshock of the 2011 Tohoku Earthquake. We thank to Dr. T.
250 Yamada of Ibaraki University, Dr. A. R. Gusman of the University of Tokyo and Dr. M.
251 Matsumura of Nagoya University for useful comments. This work was supported by JSPS
252 KAKENHI Grant Number JP 17H02062. Dr. C. H. Chen was supported by Ministry of Science
253 and Technology (MOST) of Taiwan to National Cheng Kung University under MOST-107-
254 2111-M-006-002-MY3.

255 **References**

256 Arai, N., M. Iwakuni, S. Watada, Y. Imanishi, T. Murayama, and M. Nogami (2011),
257 Atmospheric boundary waves excited by the tsunami generation related to the 2011 great
258 Tohoku Oki earthquake, *Geophys. Res. Lett.*, 38, L00G18, doi:10.1029/2011GL049146.

259 Astafyeva, E., P. Lognonné, and L. Rolland (2011), First ionospheric images of the seismic fault
260 slip on the example of the Tohoku-oki earthquake, *Geophys. Res. Lett.*, 38, L22104,
261 doi:10.1029/2011GL049623.

262 Astafyeva, E., and K. Shults (2019), Ionospheric GNSS imagery of seismic source: Possibilities,
263 difficulties, and challenges. *J. Geophys. Res.*, 124, 534–543, doi:
264 /10.1029/2018JA026107.

265 Astafyeva, E (2019), Ionospheric detection of natural hazard, *Rev. Geophys*., 57, 1265-1288,
266 doi:10.1029/2019RG00668.

267 Bolt, B. A (1964), Seismic air waves from the great 1964 Alaskan earthquake, Nature, 202,
268 1095-1096.

269 Chum, J., F. Hruska, J. Zednik, and J. Lastovicka (2012), Ionospheric disturbances (infrasound
270 waves) over the Czech Republic excited by the 2011 Tohoku earthquake, *J. Geophys.*
271 *Res.*, 117, A08319, doi:10.1029/2012JA017767.

272 Ducic, V., J. Artru, and P. Lognonné (2003), Ionospheric remote sensing of the Denali
273 earthquake Rayleigh surface waves, *Geophys. Res. Lett.*, 30 (18), 1951,
274 doi:10.1029/2003GL017812.

275 Garcia, R., F. Crespon, V. Ducic, and P. Lognonné (2005), Three-dimensional ionospheric
276 tomography of post-seismic perturbations produced by the Denali earthquake from GPS
277 data, *Geophys. J. Int.*, 163, 1049–1064, doi: 10.1111/j.1365-246X.2005.02775.x.

278 Gusman, A. R., M. Fukuoka, Y. Tanioka, and S. Sakai (2013), Effect of the largest foreshock
279 (Mw7.3) on triggering the 2011 Tohoku earthquake (Mw 9.0), *Geophys. Res. Lett*., 40,
280 497–500, doi:10.1002/grl.50153.

Hedin, A. E., E. L. Fleming, A. H. Manson, F. J. Schmidlin, S. K. Avery, R. R. Clark, S. J. Franke, G. J. Fraser, T. Tsuda, F. Vial, and R.A. Vincent (1996), Empirical wind model for the upper, middle and lower atmosphere, *J. Atmos. Terr. Phys*. 58, 1421-1447.

Kakinami, Y., M. Kamogawa, Y. Tanioka, S. Watanabe, A. R. Gusman, J.-Y. Liu, Y. Watanabe, and T. Mogi (2012), Tsunamigenic ionospheric hole, *Geophys. Res. Lett.*, 39, L00G27, doi:10.1029/2011GL050159.

Kakinami, Y., M. Yamamoto, C.-H. Chen, S. Watanabe, C. Lin, J.-Y. Liu, and H. Habu (2013a), Ionospheric disturbances induced by a missile launched from North Korea on 12 December 2012, *J. Geophys. Res.*, 118, doi:10.1002/jgra.50508.

Kakinami, Y., M. Kamogawa, S. Watanabe, M. Odaka, T. Mogi, J.-Y. Liu, Y.-Y. Sun, and T. Yamada (2013b), Ionospheric ripples excited by superimposed wave fronts associated with Rayleigh waves in the thermosphere, *J. Geophys. Res.*, 118, 905–911, doi:10.1002/jgra.50099.

Kihara, D., M.-Y. Yamamoto, T. Morinaga, A. Hatakeyama, Y. Manabe, J. Furumoto, Y. Kakinami, and T. Abe (2014), In-situ measurement of acoustic wave propagation characteristics in middle and upper atmosphere by PDI on-board S-310-41 sounding rocket, *Transactions of the Japan Society for Aeronautical and Space Sciences, Aerospace Technology Japan*, Vol. 12, No. ists29, pp. Pm_1-Pm_6.

Landau, L. D. and E. M. Lifshitz, (1959), *Fluid Mechanics, 3rd edition, chapter Ⅷ,* Pergamon Press.

Leonard, R. S., and R. A. Barns, Jr. (1965), Observation of ionospheric disturbances following the Alaska earthquake, *J. Geophys. Res.*, 70, 1250-1253.

Liu, J. Y., C.-H. Chen, C.-H. Lin, H.-F. Tsai, C.-H. Chen, and M. Kamogawa (2011), Ionospheric disturbances triggered by the 11 March 2011 M9.0 Tohoku earthquake, J. Geophys. Res., 116, A06319, doi:10.1029/2011JA016761.

Liu, J. Y., C. H. Chen, Y. Y. Sun, C. H. Chen, H. F. Tsai, H. Y. Yen, J. Chum, J. Lastovicka, Q. S. Yang, W. S. Chen, and S. Wen (2016), The vertical propagation of disturbances triggered by seismic waves of the 11 March 2011 M9.0 Tohoku earthquake over Taiwan, *Geophys. Res. Lett.*, 43, 1759–1765, doi:10.1002/2015GL067487.

Maeda, J., and K. Heki (2014), Two-dimensional observations of midlatitude sporadic E irregularities with a dense GPS array in Japan, *Radio Sci.*, 49, doi:10.1002/2013RS005295.

Maruyama, T., and H. Shinagawa (2014), Infrasonic sounds excited by seismic waves of the 2011 Tohoku-oki earthquake as visualized in ionograms, *J. Geophys. Res.*, 119, 4094–4108, doi:10.1002/2013JA019707.

Nishitani, N., T. Ogawa, Y. Otsuka, K. Hosokawa, and T. Hori (2011), Propagation of large amplitude ionospheric disturbances with velocity dispersion observed by the SuperDARN Hokkaido radar after the 2011 off the Pacific coast of Tohoku Earthquake, *Earth Planets Space*, 63, 891–896.

Occhipinti, G., L. Rolland, P. Lognonné, and S. Watada (2013), From Sumatra 2004 to Tohoku-Oki 2011: The systematic GPS detection of the ionospheric signature induced by tsunamigenic earthquakes, *J. Geophys. Res*., 118, 3626–3636, doi:10.1002/jgra.50322.

Ozeki, M. and K. Heki, Ionospheric holes made by ballistic missiles from North Korea detected with a Japanese dense GPS array (2010), *J. Geophys. Res.*, 115, A09314, doi:10.1029/2010JA015531.

Picone, J. M., A. E. Hedin, D. P. Drob, and A. C. Aikin (2002), NRLMSISE-00 empirical model of the atmosphere: Statistical comparisons and scientific issues, *J. Geophys. Res.*, 107, 1468, doi:10.1029/2002JA009430.

Pierce, A. D., (2007), Basic Liner Acoustics, in: Rossing, T.D. (Ed.), *Springer Handbook of Acoustics*, chap. 3, New York: Springer.

Stroud, W. G., W. Nordgerg, W. R. Bandeen, F. L. Bartman, and P. Titus (1960), Rocket-Grenade Measurements of Temperatures and Winds in the Mesosphere over Churchill, Canada, *J. Geophys. Res.*, 65, 2307-2323.

Thomas, D., M. S. Bagiya, P. S. Sunil, L. Rolland, A. S. Sunil, T. D. Mikesell, S. Nayak, S. Mangalampalli and D. S. Ramesh (2018), Revelation of early detection of coseismic ionospheric perturbations in GPS-TEC from realistic modelling approach: Case study, *Scientific Reports*, 8(1), 12105, doi:10.1038/s41598-018-30476-9.

Figure 1. An example of the raw and filtered slant total electron content (TEC) observed at the station 0940 for the satellite PRN10. The raw data are depicted in red, 10-s-filtered in blue, and 180-s-filtered in magenta lines. The black line shows the 10-s-filtered data (blue) subtracted by the 180-s-filtered (magenta), representing 10-180-s band-pass filtered data. Here, 1 TECu = 1×10^{16} electron/m^2.

Figure 2. Schematic illustration of changing the location of the sub-ionospheric point (SIP) associated with a change in the assumed altitude.

Figure 3. (a-c) Snapshots of the spatial distribution of the filtered TEC disturbance observed by (a) PRN07, (b) PRN08, and (c) PRN10 for the assumed altitude of 300 km. The black arrows show locations of the extending CIDs. The red stars and crosses indicate the epicenter and the geographic coordinates of the onset point of the CIDs, respectively. (d-f) Time series of the 10-180-s band-pass-filtered TEC for PRN07, PRN08, and PRN10. The number attached to each line denotes the name of each station. The vertical solid red and dotted red lines denote the time of the main shock and eight minutes after the main shock, respectively. The red dots indicate the time of the first maximum of each CID, namely, the arrival time of the acoustic wave.

Figure 4. Snapshots of spatial distribution for the onset time measured from the main shock for the assumed altitude of 300 km for (a) PRN07, (b) PRN08 and (c) PRN10. The red stars and crosses indicate the epicenter and the geographic coordinates of the onset point, respectively.

Figure 5. Scatter plot of the arrival time of the acoustic wave from the main shock versus the distance between the geographic coordinates of the tentative onset points and SIPs for the altitude of 155 km for PRN07. The red line is a best-fitted line determined by using the least-squares fit.

Figure 6. Geographic coordinates of the onset points for several tentative altitudes. Here, we show 150, 155, 160, and 200 km for PRN07 (red), and 200, 230, 235, and 240 km for PRN10 (blue). The crosses show the geographic coordinates of the onset points for the tentative altitudes given above. The intersection of the red and blue lines is the geographic coordinates of the coinciding point of the onset points determined in the present analysis.

Figure 7. Spatial distribution of the arrival time of the acoustic wave (a) at 155 km for PRN07 and (b) at 235 km for PRN10. The red stars and crosses indicate the epicenter and the onset points finally determined by the present method.

Figure 8. Altitude profiles of the acoustic wave velocity (blue line) and the neutral temperature (black line) based on NRLMSISE-00. The red dot denotes the acoustic wave velocity averaged over the altitudes of 155 and 235 km determined in the present study. The horizontal and vertical error bars display respectively, the errors in the velocity and the altitude resulting from the ambiguity in the altitude (see the text). The blue dashed line displays the altitude profile of the acoustic wave velocity for the neutral temperature twice the model values.

Figure 9. Configuration of the onset points of the CID, the satellites, the acoustic wave, and the source of the acoustic wave. The disturbance was detected earlier by PRN07 at a lower elevation angle, and later by PRN10 at a higher elevation angle. The filled red ovals denote the onset points at the altitude shown in the figures.

379 **Figure 10**. Altitude profile of attenuation of the amplitude of the acoustic waves of frequencies
380 between $f = 10^{-2}$ and 10 Hz calculated using NRLMSISE-00. Acoustic waves suffer rapid
381 attenuation and cannot propagate above the altitude of $\alpha\lambda > 1$, where α is the absorption
382 coefficient and λ is the wavelength.

Figure 1.

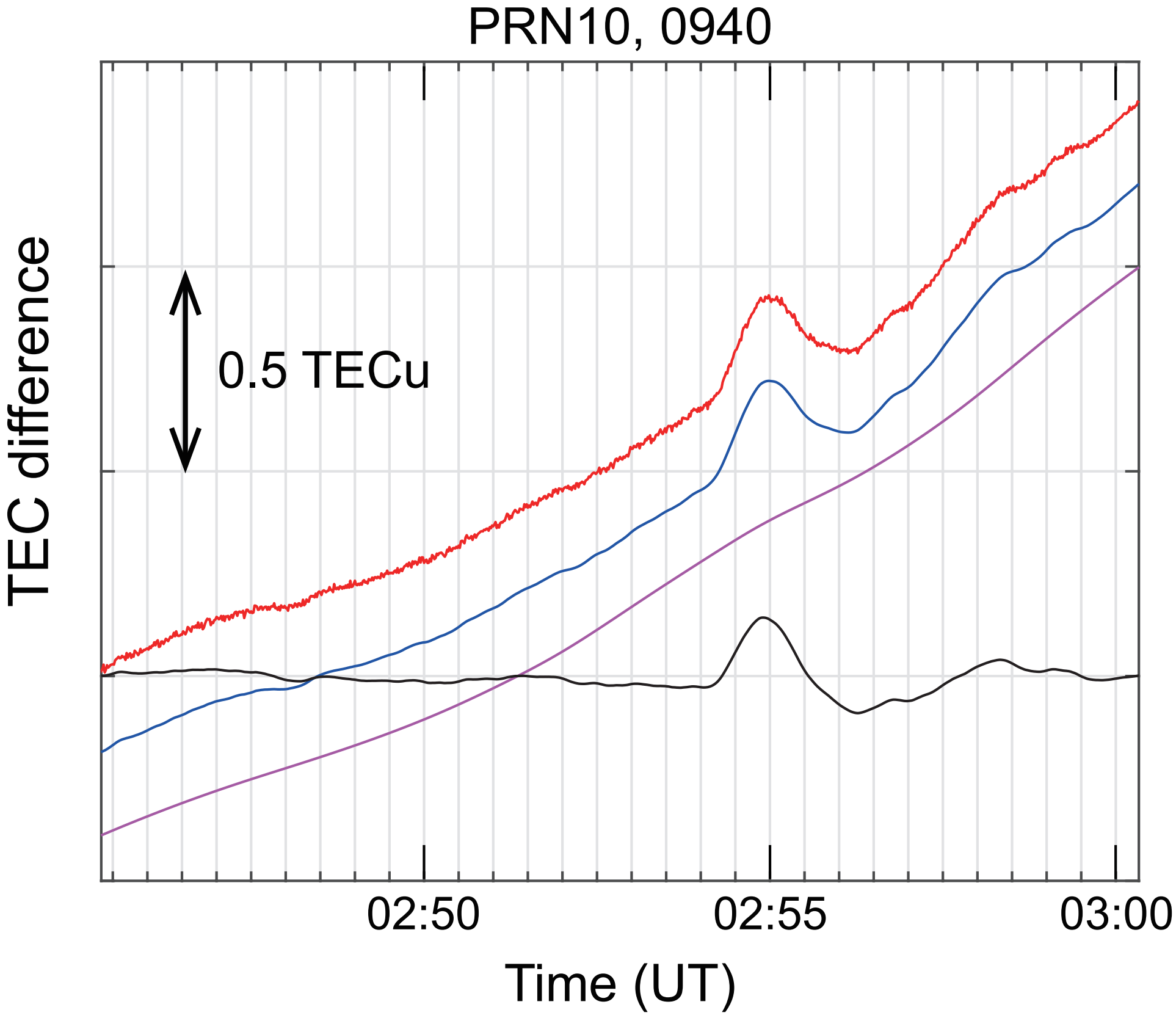
PRN10, 0940
TEC difference
0.5 TECu
02:50
02:55
03:00
Time (UT)

Figure 2.

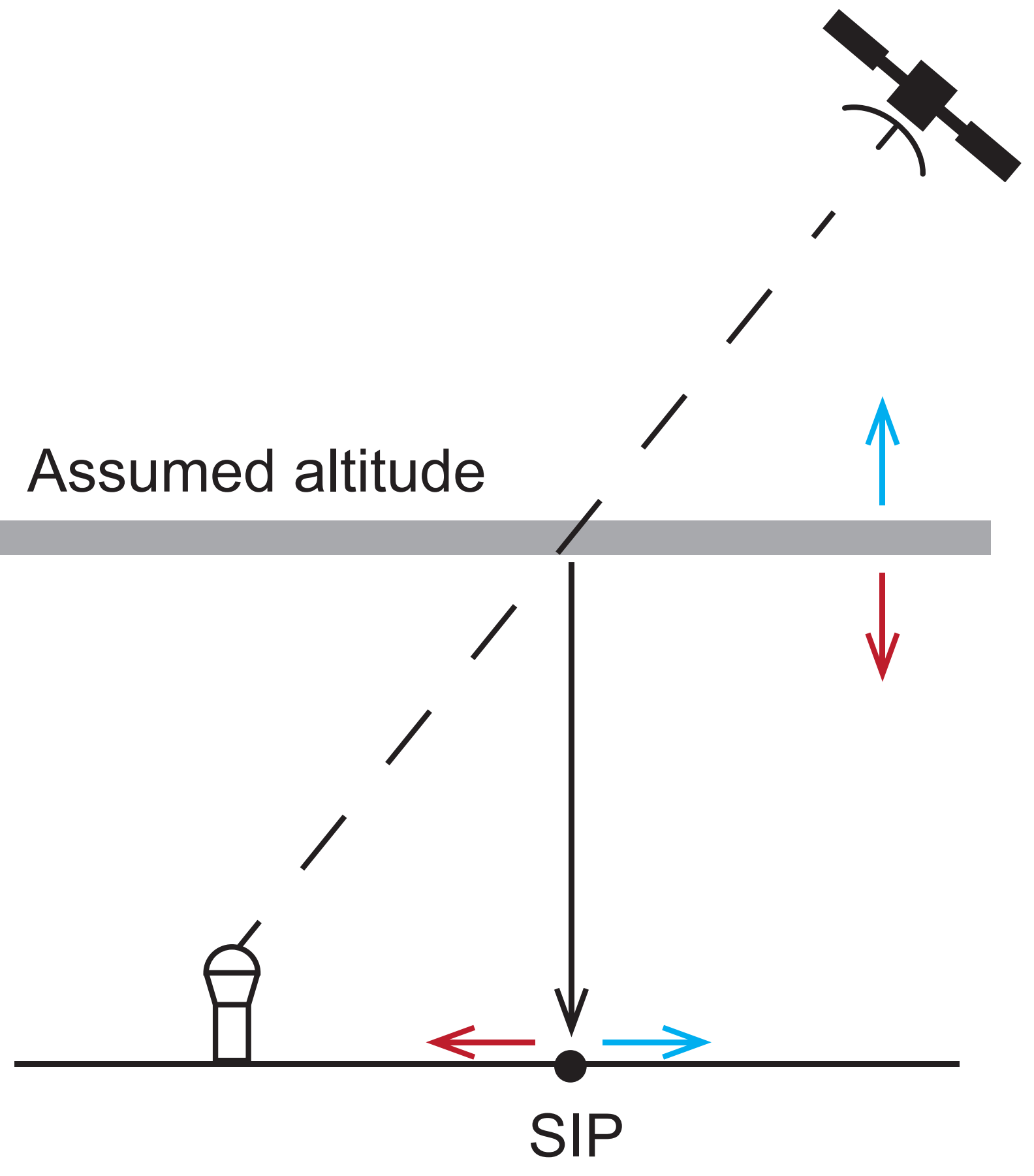
Assumed altitude
SIP

Figure 3.

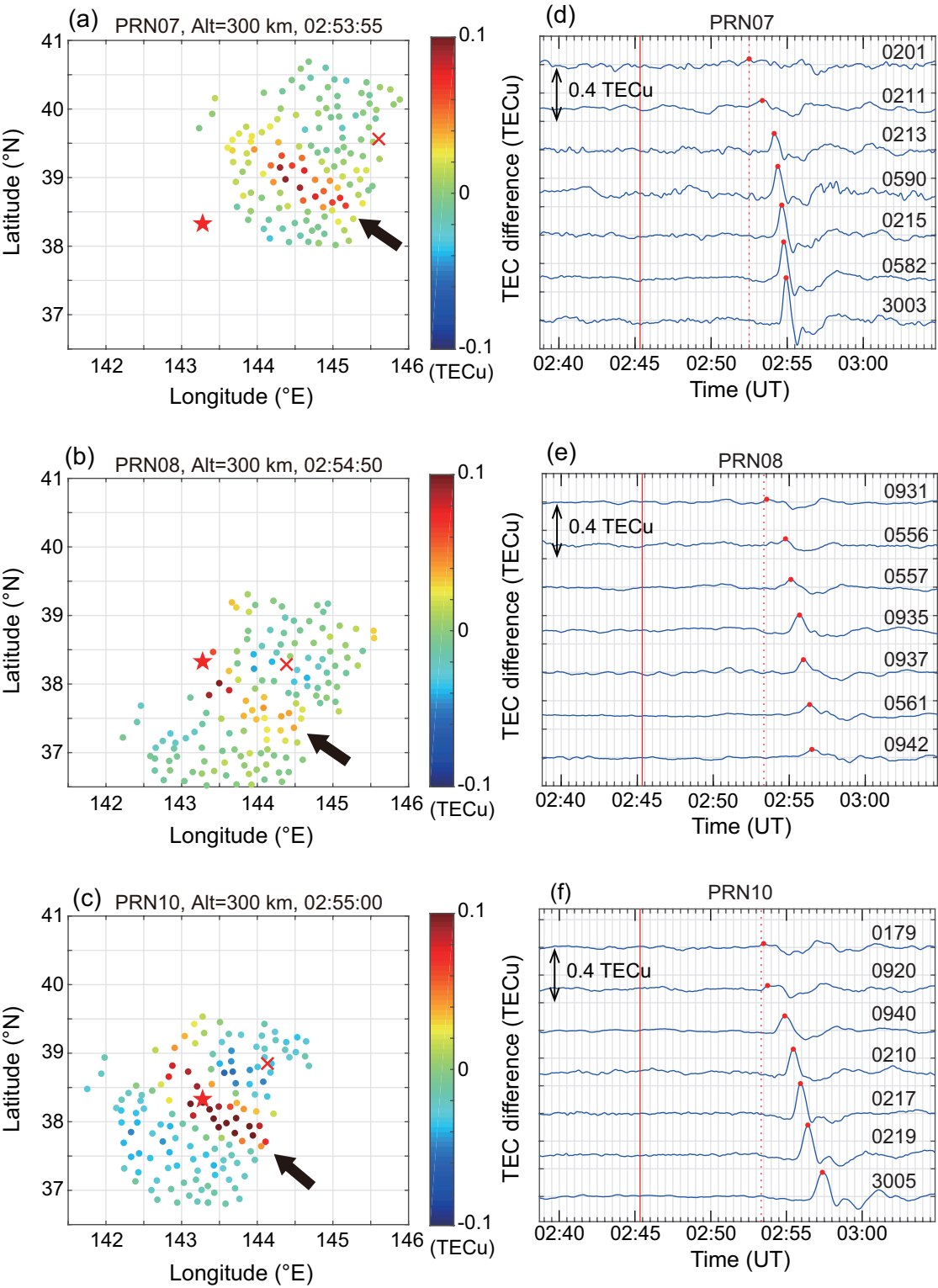
(a)
PRN07, Alt=300 km, 02:53:55
Latitude (°N)
Longitude (°E)
(TECu)
(b)
PRN08, Alt=300 km, 02:54:50
(c)
PRN10, Alt=300 km, 02:55:00
(d)
PRN07
(e)
PRN08
(f)
PRN10
TEC difference (TECu)
0.4 TECu
Time (UT)
0201
0211
0213
0590
0215
0582
3003
0931
0556
0557
0935
0937
0561
0942
0179
0920
0940
0210
0217
0219
3005

Figure 4.

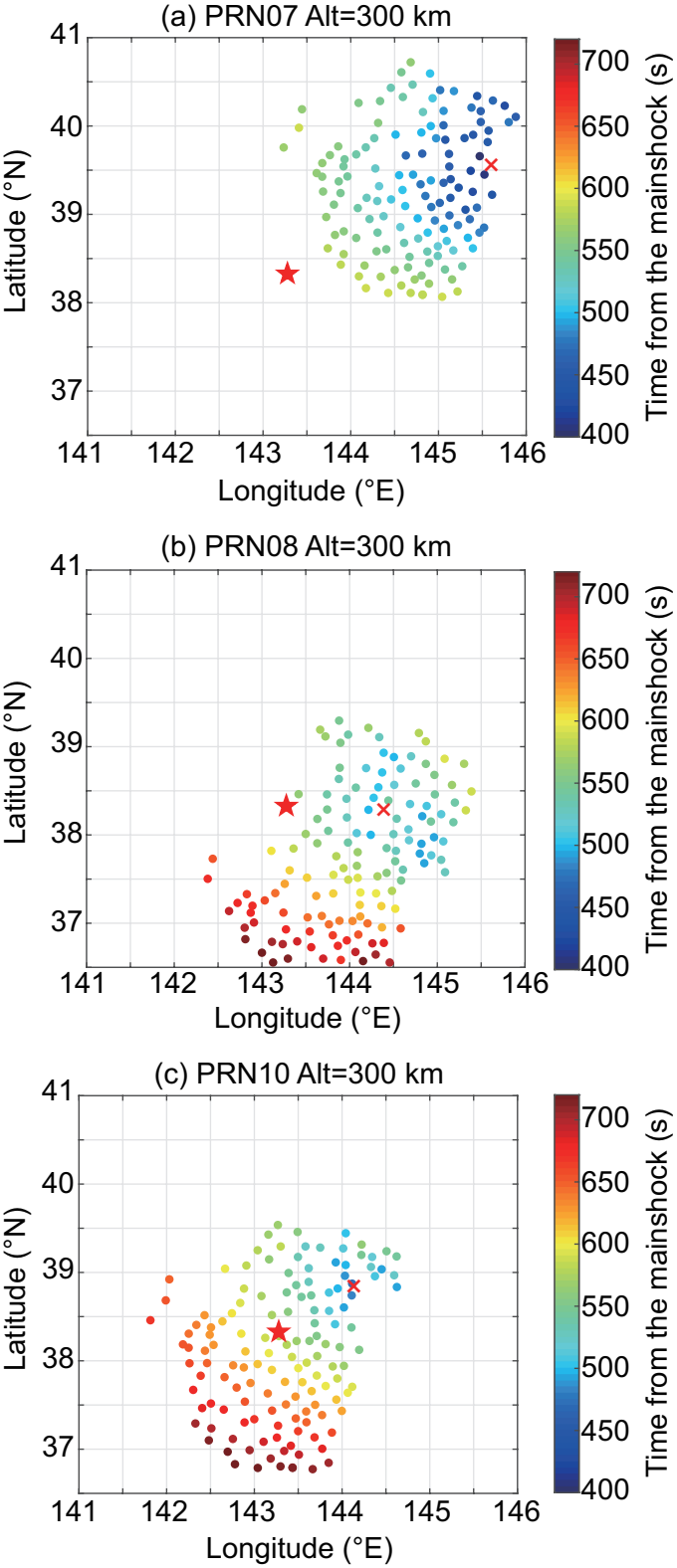
(a) PRN07 Alt=300 km
(b) PRN08 Alt=300 km
(c) PRN10 Alt=300 km
Latitude (°N)
Longitude (°E)
Time from the mainshock (s)
41
40
39
38
37
141
142
143
144
145
146
700
650
600
550
500
450
400

Figure 5.

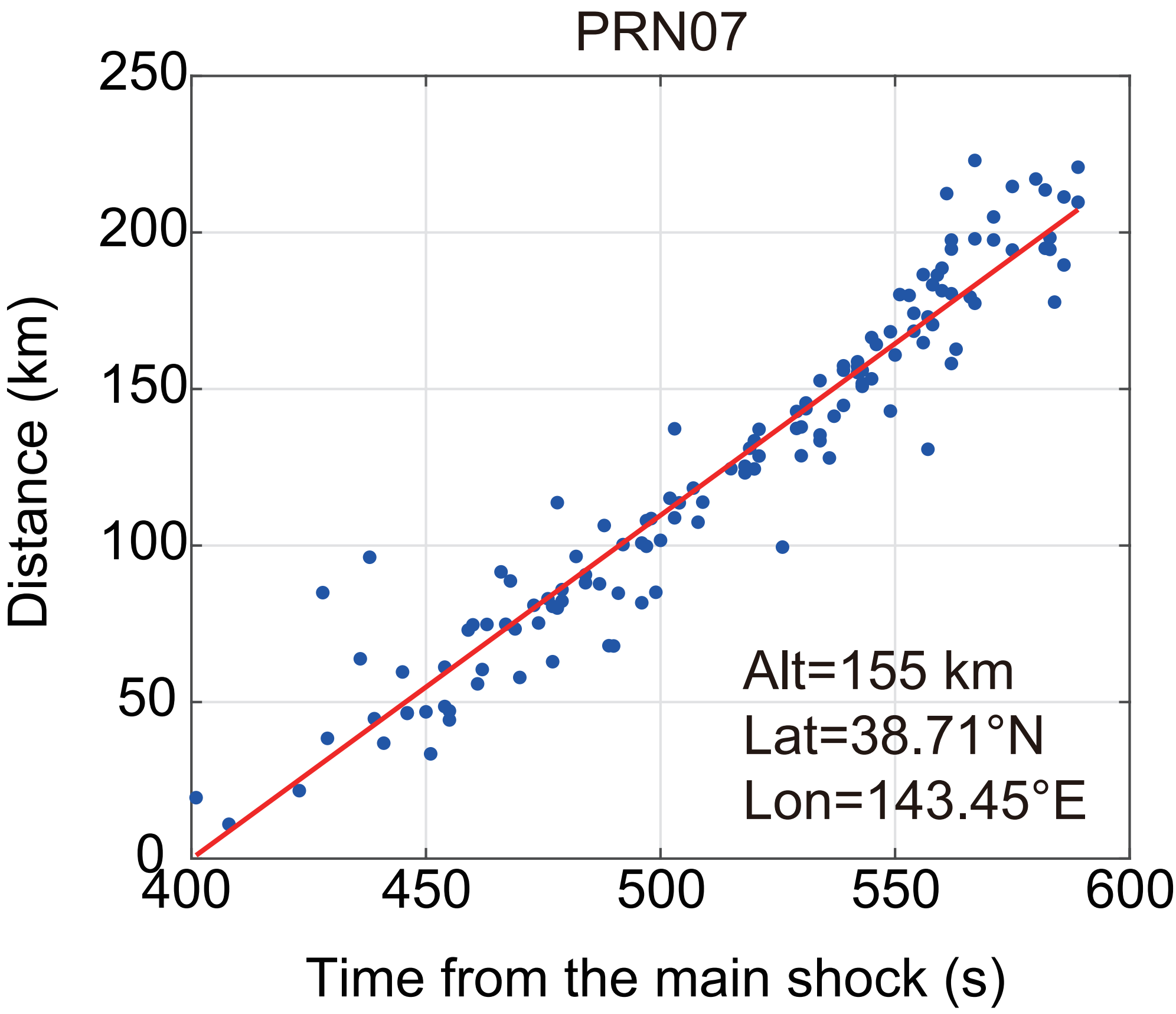
PRN07
250
200
150
100
50
0
Distance (km)
400
450
500
550
600
Time from the main shock (s)
Alt=155 km
Lat=38.71°N
Lon=143.45°E

Figure 6.

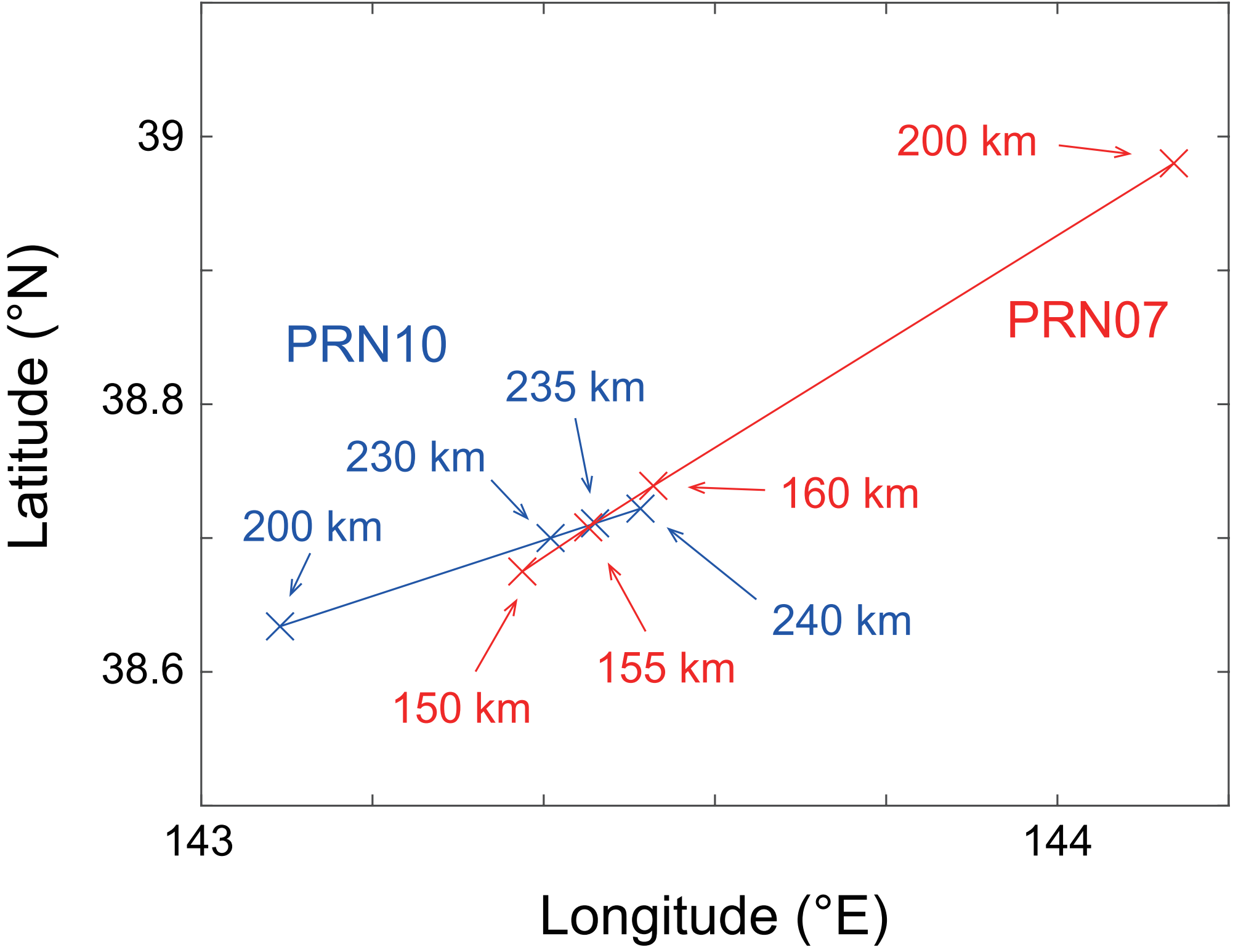
39
38.8
38.6
143
144
Latitude (°N)
Longitude (°E)
PRN10
PRN07
200 km
235 km
230 km
200 km
160 km
240 km
155 km
150 km

Figure 7.

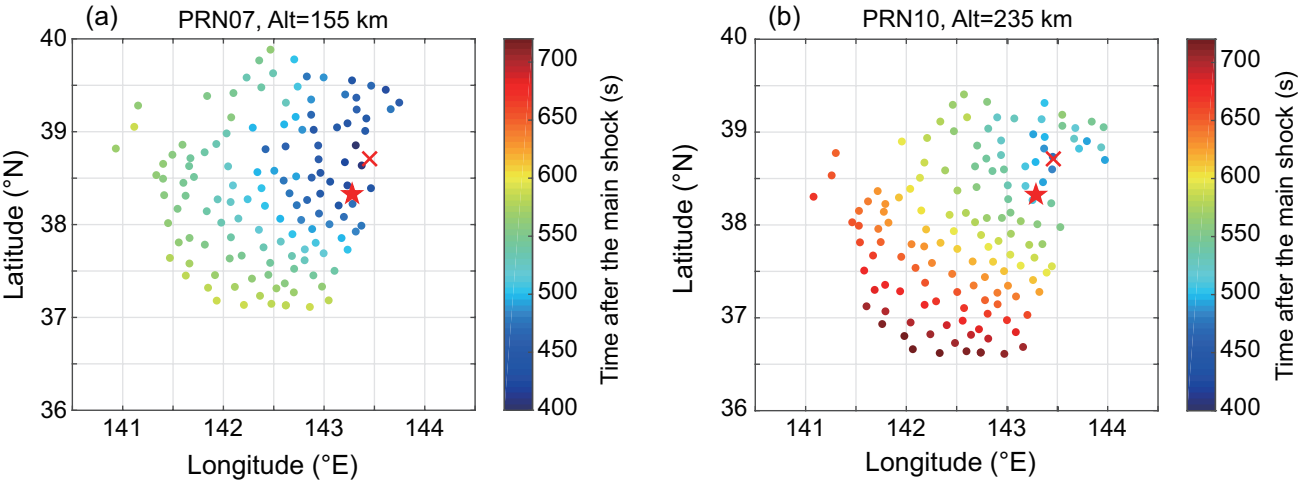
(a)
PRN07, Alt=155 km
Latitude (°N)
Longitude (°E)
Time after the main shock (s)
(b)
PRN10, Alt=235 km
Latitude (°N)
Longitude (°E)
Time after the main shock (s)

Figure 8.

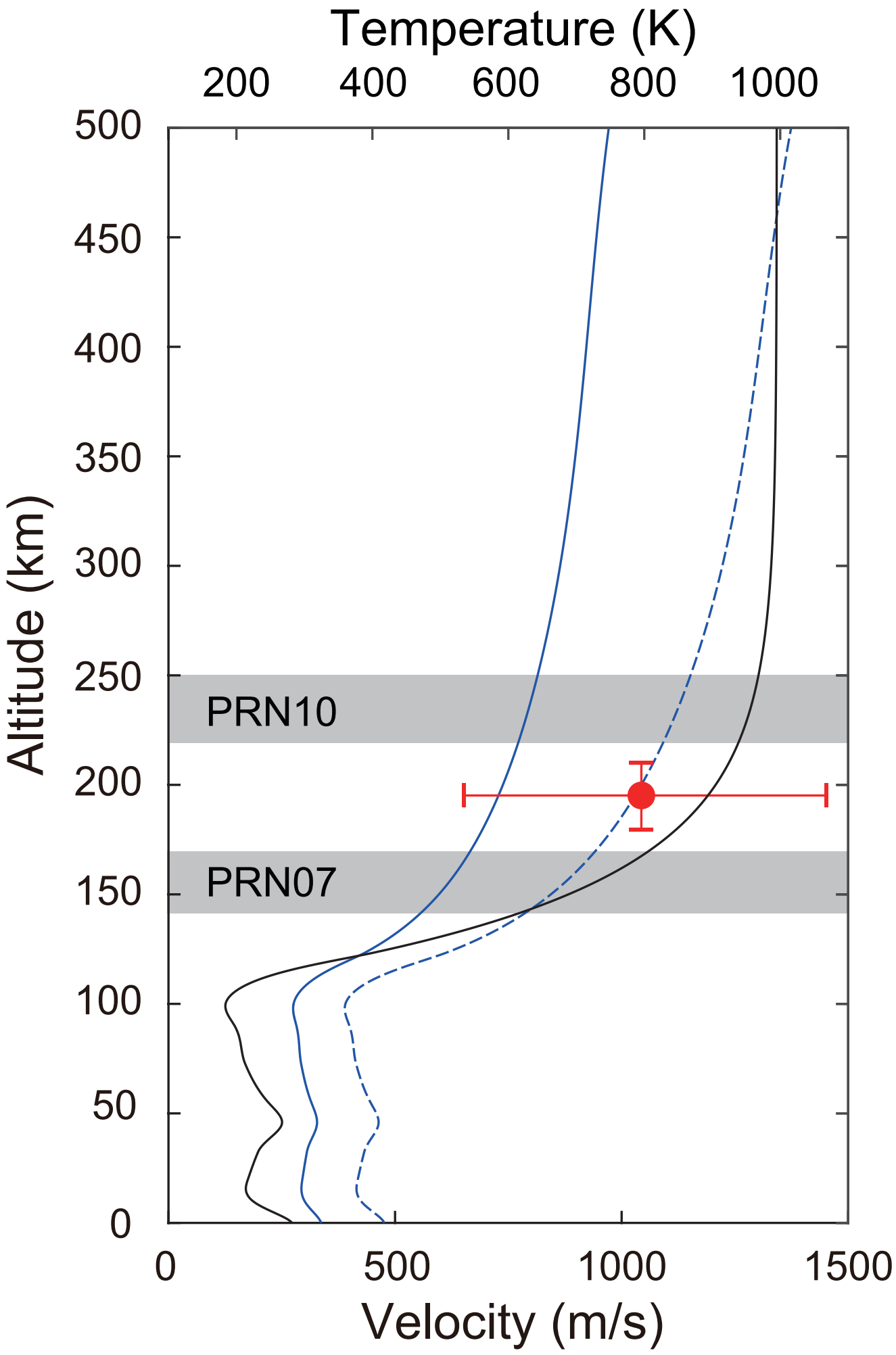
Temperature (K)
200
400
600
800
1000
500
450
400
350
300
250
200
150
100
50
0
Altitude (km)
PRN10
PRN07
0
500
1000
1500
Velocity (m/s)

Figure 9.

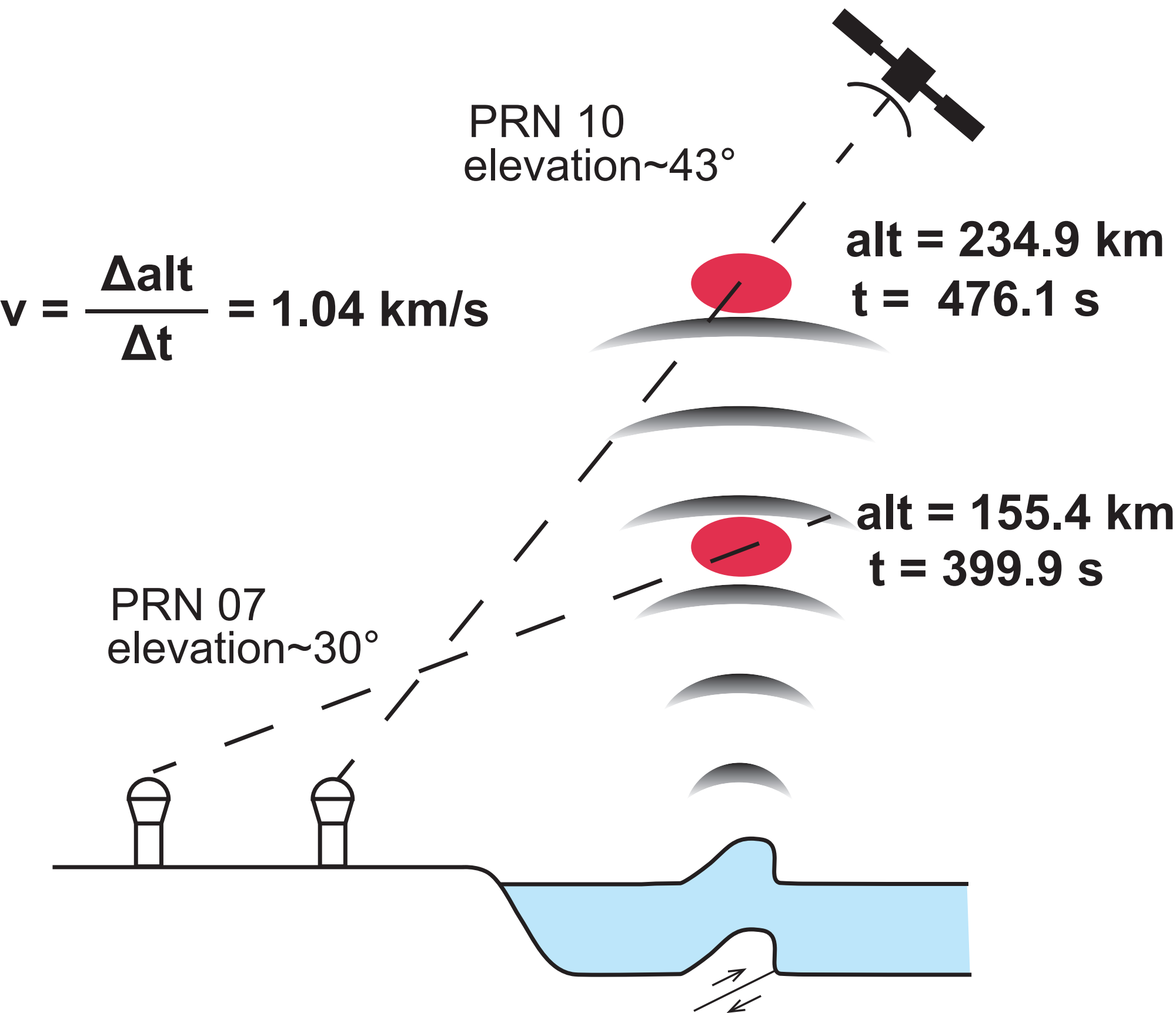
PRN 10
elevation~43°
alt = 234.9 km
t = 476.1 s
$v = \frac{\Delta alt}{\Delta t} = 1.04$ km/s
alt = 155.4 km
t = 399.9 s
PRN 07
elevation~30°

Figure 10.

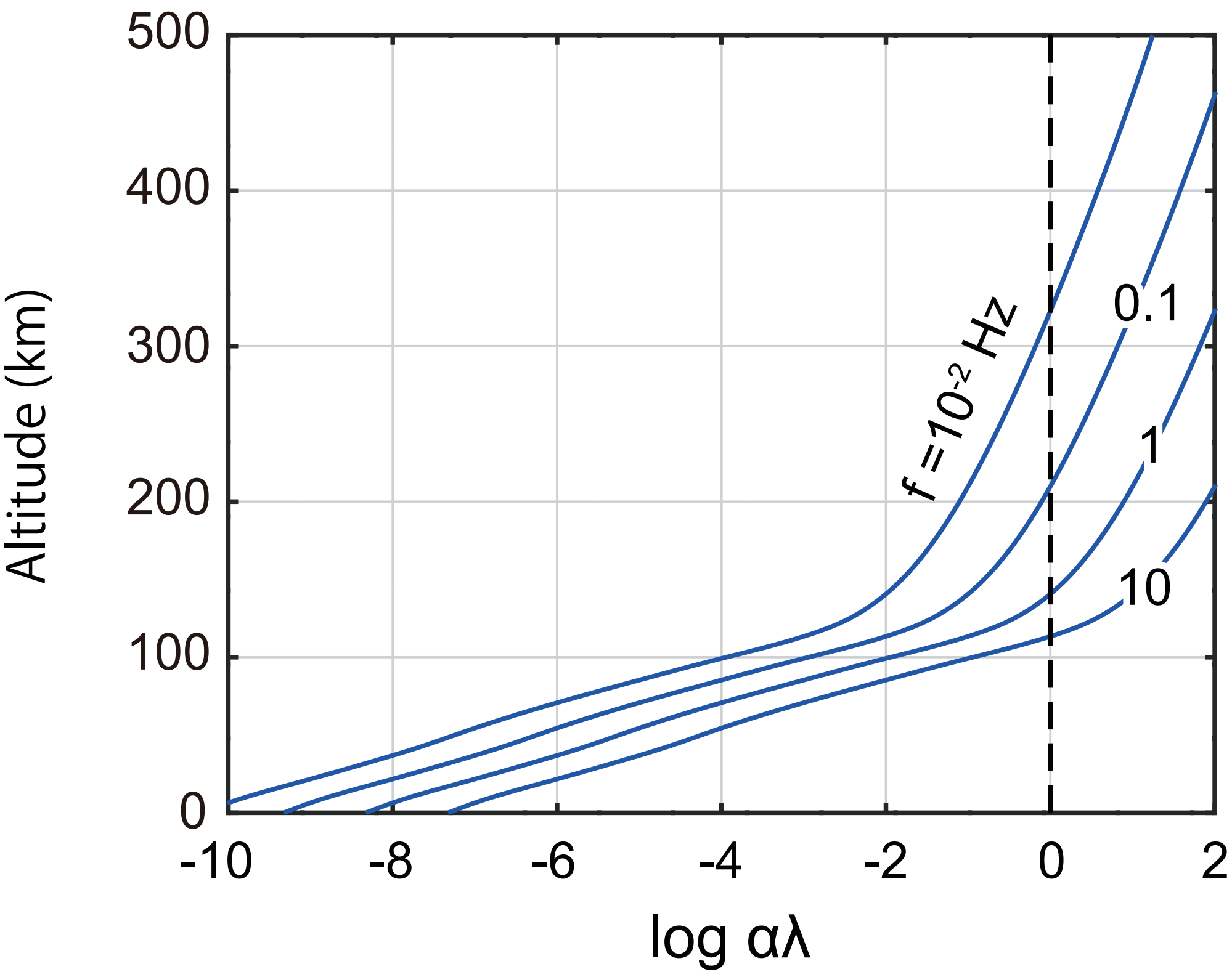
500
400
300
200
100
0
Altitude (km)
-10
-8
-6
-4
-2
0
2
log αλ
f =10-2 Hz
0.1
1
10